Chemical Engineering Journal 425 (2021) 131608

Contents lists available at ScienceDirect

Chemical Engineering Journal

journal homepage: www.elsevier.com/locate/cej

High electromagnetic wave absorption and thermal management performance in 3D CNF@C-Ni/epoxy resin composites

Yongxin Qian, Yang Tao, Wang Li, You Li, Tian Xu, Jinian Hao, Qinghui Jiang, Yubo Luo *, Junyou Yang *

State Key Laboratory of Materials Processing and Die & Mould Technology, Huazhong University of Science and Technology, Wuhan 430074, PR China

ARTICLE INFO

Keywords:
Epoxy resin
Carbon nanofibers
Electromagnetic wave absorption
Thermal management

ABSTRACT

Electronic packaging materials with efficient heat dissipation and anti-electromagnetic-interference performance are highly desirable to realize the long-term stable operation of highly integrated electronic devices. Such combined functions of heat dissipation and anti-electromagnetic-interference are achieved here by filling 3D CNF@C-Ni network skeleton in epoxy resins (EP). The CNF@C-Ni is a carbon nanofibers network skeleton embedded with micron flower-like C-Ni particles and has been obtained by carbonizing nickel metal–organic frameworks (Ni-MOF) embellished bacterial cellulose. The 3D CNF@C-Ni network skeleton provides a highly efficient heat transfer channel for EP, rendering a high thermal conductivity of 0.5 $W{\cdot}m^{-1}K^{-1}$ at room temperature for the 5 wt% CNF@C-Ni filled EP, ~2.8 times higher than that of pristine EP. In addition, the flower-like C-Ni particles realize an optimization in the impedance matching of CNF@C-Ni/EP, enabling a high electromagnetic wave absorption performance in the wave-transparent epoxy resins. In particular, a lowest reflection loss value of −49.77 dB at 13.44 GHz with a maximum effective bandwidth of 5.44 GHz (from 12.08 to 17.52 GHz) has been achieved in the 5 wt% CNF@C-Ni filled epoxy resins with a thickness of 2.2 mm. Such a new dual-functionated epoxy resin with combined high electromagnetic wave absorption and thermal management performance shows great potential in manufacturing of highly integrated electronic devices.

1. Introduction

Packaging materials serve as a key component for electronic devices, which offer heat dissipative pathways for electronic circuits [1,2] and keep them away from environmental effects (e.g., humidity, chemicals and radiation) [3,4]. Electronics packaging materials encompass a wide range of objects, including ceramics [5], metals [6], polymers [7] and so on. Among them, polymers, especially epoxy resins, are intensively used today because of their easy processibility, low cost, high electrical resistance, corrosion resistance and mechanical strength [8–11]. However, the intrinsically low thermal conductivity (e.g., ~0.2 $W{\cdot}m^{-1}K^{-1}$ at room temperature) [12] of epoxy resins derived from their amorphous polymer chains makes itself difficult to quickly dissipate the heat created by electronic devices. Thus, the application of epoxy resins for packaging of highly integrated and high-power density electronic devices is largely limited. In addition, the electromagnetic interference has gradually become serious due to the broad application of high-frequency electromagnetic waves (EMW) in both civil and military fields (e.g., 5G/6G wireless communication systems) [13,14]. Unfortunately, most of the epoxy resins are good EMW transmitting materials, namely they cannot attenuate the unwanted EMW thus keeping the electronic devices away from the EM interference problems. Therefore, epoxy resins with good electromagnetic waves absorption and thermal conductivity are highly desired in packaging of highly integrated and high-power density electronic devices, which have attracted increasing attentions from the academic and industrial fields.

In order to improve the thermal conductivity of epoxy resins, high thermal conductive materials (e.g., SiO_2, AlN, BN, and Al_2O_3) have been filled into epoxy resins [15–17]. Meanwhile, the size distribution and orientation of the fillers as well as the interface tailoring between the filler and the polymer matrix have also been intensively studied and optimized [18–20]. Enhanced thermal conductivity has been obtained in the fillers/epoxy resins composites with a high filler content. For example, the thermal conductivity of 40% SiO_2 filled epoxy resins reaches 0.4 $W{\cdot}m^{-1}K^{-1}$ at room temperature, 122% higher than that of pure epoxy resins [21]. It is noted that such a high filling content will

* Corresponding authors.
E-mail addresses: luoyubo@hust.edu.cn (Y. Luo), jyyang@mail.hust.edu.cn (J. Yang).

https://doi.org/10.1016/j.cej.2021.131608
Received 26 June 2021; Received in revised form 23 July 2021; Accepted 27 July 2021
Available online 10 August 2021

significantly increase the density of epoxy resins, violating the requirement of light weight for highly integrated micro-electronic devices. Thereby, carbon-based fillers (e.g., graphite, graphene, 3D carbon skeleton) are highly desirable because of their low density and high electrical conductivity [22]. In which, graphene is widely studied due to its high thermal conductivity of ~4000 $W \cdot m^{-1}K^{-1}$ at room temperature [23]. But the graphene/epoxy resins composition has significantly anisotropic thermal conductivities, thus an isotropic three-dimensional skeleton is an emerging strategy to optimize the thermal conductivity of epoxy resins [24,25]. For example, the 3D thermal conductivity of the graphene and sponge composite [26] is up to 2.19 $W \cdot m^{-1}K^{-1}$. However, the complex preparation process and high cost of graphene largely limit its applications. Therefore, developing alternative 3D thermally conductive carbon skeleton fillers lies in the core of EP packaging materials research.

In addition to the heat dissipation requirement, reducing the electromagnetic waves interference to electronic devices is also an urgent requirement for epoxy resins based electronic packaging materials. However, the electromagnetic waves absorption performance of pure carbon materials itself is relatively low due to the poor impedance matching/mismatched impedance [27–29], thus the epoxy resins filled with pure carbon materials also show poor electromagnetic waves absorption performance. Recently, surface modification and the three-dimensional structure design have been carried out to enhance impedance matching and electromagnetic wave loss [30–33].In particular, the minimum reflection loss (RL) of the NiAl layered double hydroxide/graphene (NiAl-LDH/G) 3D composite material is −41.5 dB, and its effective absorption bandwidth reaches 4 GHz [34]. Unfortunately, such performance is still, or the thermal conductivity of the NiAl-LDH/G is low. How to enhance the thermal performance and extend the electromagnetic waves absorption performance of epoxy resins as much as possible is still a big challenge needed to be resolved.

Herein, we introduce an epoxy resin filled with 3D carbon nanofibers embedded with micron flower-like C-Ni particles (i.e., CNF@C-Ni/EP) as a promising candidate for dual-functionalized electronic packaging materials. A natural, non-toxic, low-cost biological material, bacterial cellulose (BC), has been employed as the precursor of 3D carbon skeleton, because of its high aspect ratio and good 3D carbon network after carbonization [35–38]. Nickel metal–organic frameworks (Ni-MOF) with a size of ~2 μm has been grown on the surface of bacterial cellulose (BC) using a hydrothermal reaction. The 3D CNF fillers are obtained by carbonizing BC at 900 °C, and amorphous C and nanoscale Ni particles are formed on the surface of CNF, (i.e., CNF@C-Ni). The CNF@C-Ni/EP composites with a thickness of 1.8 mm are obtained by vacuum impregnation method. In which, the CNF@C-Ni reserves the 3D skeleton of 3D CNF, which serves as the heat propagation path in CNF@C-Ni/EP composite. The thermal conductivity of CNF@C-Ni/EP reaches ~0.5 $W \cdot m^{-1}K^{-1}$ with an ultralow filling content of CNF@C-Ni (5 wt%), double the value of pure epoxy resin. Meanwhile, the introduction of CNF@C-Ni into epoxy resin enhances the impedance matching between CNF@C-Ni/epoxy resin composites and air, and causes more interface polarization in the composites. It enables us to achieve a high reflection loss value of −49.77 dB combined with an effective bandwidth of 5.44 GHz. The high thermal conductivity and EMW absorbing performance indicate that our dual-functionalized CNF@C-Ni/epoxy resin composite is highly desirable for electronic packaging application.

2. Experimental section

2.1. Materials

Bacterial cellulose (BC) membranes were provided by Hainan Yide Foods Co., Ltd, China. NaOH and dimethylformamide (DMF) were obtained from Sinopharm Chemical Reagent Co., LTD. Nickel nitrate hexahydrate ($Ni(NO_3)_2 \cdot 6H_2O$) was purchased from Shanghai Aladdin Industrial Corporation. p-Phthalic acid was purchased from Shanghai Macklin Biochemical Technology Co., Ltd. All reagents mentioned above were of analytical grade and used without any further purification.

2.2. Pretreatment of BC

Dipped BC membranes in a 0.5 M NaOH solution (80 °C) and stirred for 6 h to remove impurities in the BC, and then washed the BC with deionized water until pH of washing solution was about 7. Finally freeze-dried washed BC at −45 °C, 1 Pa for 48 h, and samples thus obtained were denoted as BC.

2.3. Synthesis of BC@Ni-MOF

BC decorated by Nickel metal–organic frameworks (Ni-MOF) were obtained by a simple hydrothermal reaction. First, x mg (x = 200, 400, 600) of $Ni(NO_3)_2 \cdot 6H_2O$ and 200 mg of BC were immersed in 70 ml DMF solution, the obtained mixture was magnetically stirred at 40 °C for 1 h. Then 70 mg, 140 mg, 210 mg p-Phthalic acid were added into the mixture respectively followed by stirring for 30 min. The precursor solution was transferred to an autoclave lined with Teflon (150 °C, 3 h). Hereafter, the product was washed with deionized water and ethanol to remove residual impurities and DMF in BC. At last, the samples were freeze-dried at −45 °C, 1 Pa for 48 h. The samples thus obtained were denoted as BC@Ni-MOF (200, 400, 600).

2.4. Preparation of CNF and CNF@C-Ni

The freeze-dried BC and BC@Ni-MOF were processed under Ar atmosphere at 900 °C for 2 h to obtain CNF and CNF@C-Ni, respectively. The obtained samples were denoted as CNF, CNF@C-Ni (200), CNF@C-Ni (400), CNF@C-Ni (600), respectively.

2.5. Preparation of CNF@C-Ni/EP composites

95 mg CNF@C-Ni was placed in a special mold, then slowly added 100 mg of epoxy resin (EP) precursor. (provided by Changshu Jiafa Chemical Co., Ltd.), the sample was then transferred to a vacuum drying oven for forming process at 120 °C, 1 Pa. Similarly, as a comparison, pure EP tablets were also prepared under the same process. The thickness of the CNF@C-Ni/EP was 1.8 mm.

2.6. Characterization and measurements

The microscopic morphologies of BC, BC@Ni-MOF, CNF and CNF@C-Ni were characterized by Scanning Electron Microscopy (Gemini SEM 300). The electromagnetic data including the relative permittivity and permeability of the samples were obtained with with the transmission/reflection coaxial line method by a vector network analyzer in 2–18 GHz, Agilent (N5244A). The specimens used for evaluating the electromagnetic properties were prepared by dipping 5 wt% CNF@C-Ni into epoxy resin, a toroid with outer diameter of 7.00 mm, inner diameter of 3.04 mm and thickness of 2 mm. The Nitrogen adsorption–desorption curves were obtained by specific surface area analyzer (Micromeritics ASAP2020), Brunauer-Emmett-Teller method and Barrett-Joyner-Halenda method were used to analyze specific surface area and pore size distribution of samples respectively. The crystal structure of the sample was analyzed by X-ray diffraction (XRD) on a PANalytical B.V X-ray diffractometer. The sample composition was studied in air atmosphere at a heating rate of 10 °C/min by using Pyris1 TGA. The FTIR spectra were obtained by Nicolet iN10 spectrometer, the thermal conductivity was collected using transient hot wire method through a XIATECH TC3010 instrument. The temperature and infrared images during the heating and cooling process were recorded by an infrared thermal imaging device (FLUKE Ti480 PRO).

3. Results and discussion

3.1. Phase, microstructure and composition

The preparation process of the dual-functionalized EP with micro-scale flower-like C-Ni decorated 3D carbon nanofibers (CNF) skeleton (i.e., CNF@C-Ni/EP) is schematically shown in Fig. 1a. First, BC with a natural 3D porous structure was purchased and washed using a 0.5 M NaOH solution to remove impurities. Ni-MOF was in-situ grown on the surface of BC by hydrothermal reaction method at 150 °C. In order to study the effect of Ni-MOF content on the performance of CNF@C-Ni/EP, different masses of $Ni(NO_3)_2{\cdot}6H_2O$ (200, 400, 600 mg) were added to obtain samples with different Ni-MOF loading content, which are marked as BC@Ni-MOF (200, 400, 600) respectively. Then, high-temperature carbonization procedure at 900 °C was carried out to obtain CNF@C-Ni with a 3D network structure under an Ar atmosphere. Finally, a certain amount of EP was filled into the interspace of 3D network in CNF@C-Ni under vacuum at 120 °C.

Fig. 1b shows the X-ray diffraction patterns for BC, Ni-MOF, BC@Ni-MOF, CNF and CNF@C-Ni. The Bragg peaks of BC@ Ni-MOF (blue line) can be well index to BC and Ni-MOF, confirming that Ni-MOF has been grown on the surface BC successfully. After carbonization at 900 °C, CNF only shows a broad Bragg peak of (002) of graphite around 24° (green line), indicating partial the CNF was graphitized during carbonizing process. The XRD pattern of CNF@C-Ni (purple line), besides the Bragg peak of (002) of graphite, other Bragg peaks detected at 44.5°, 51.8° and 76.4° can be well indexed to (111), (200) and (220) planes of face-centered cubic Ni (JCPDS No. 87-0712) [39], respectively. It implies that metallic Ni was created in CNF@C-Ni owing to the decomposition of Ni-MOF, which is consistent with our EDS spectrum shown in Fig. S1. In addition, the components of BC, CNF, BC@Ni-MOF and CNF@C-Ni were analyzed by Fourier transform infrared (FTIR) spectroscopy (Fig. 1c). Compared with pure BC, BC@Ni-MOF has a clear infrared absorption peak around 816 cm^{-1}, we attribute it to the C-H in-plane bending vibration generated by the para-substitution of organic ligands in Ni-MOF, confirming the formation of Ni-MOF. After high-temperature carbonization, no obvious infrared absorption peaks can be observed in the FTIR spectra of CNF and CNF@C-Ni, implying the functional groups in BC and Ni-MOF have been eliminated during high-temperature carbonization procedure [40]. Thermogravimetric analysis (TGA) (Fig. S2) indicates the contents of Ni in CNF@C-Ni (200), CNF@C-Ni (400) and CNF@C-Ni (600) are about 18.28%, 44.33%, 66.22%, respectively.

In order to study the porous structure of the samples, we carried out N_2 adsorption–desorption measurements on CNF and CNF-C-Ni, Fig. 1d. The isotherms of CNF and CNF-C-Ni (400) show typical type-IV curves, indicating the existence of mesoporous and macroporous structures inside the samples [41,42]. Furthermore, the specific surface areas of CNF and CNF@C-Ni (400) are 372.71 and 462.94 m^2g^{-1}, respectively. Pore size distribution shows that CNF@C-Ni (400) may have a microporous structure based on Barrett-Joyner-Halenda (BJH) method (Fig. S8). It means the introduction of C-Ni porous structure could effectively increase the specific surface area of CNF. Such a high specific surface area observed in CNF@C-Ni (400) not only facilitates the multiple scattering or reflection of microwaves, thus enhancing the attenuation of microwaves (Table S1), but also greatly reduces the density of the material and adjusts impedance matching, which is beneficial to the preparation of lightweight microwave absorbers [43].

The macroscopic morphology and microstructure of BC, BC@Ni-MOF and CNF@C-Ni are shown in Fig. 2. The bacterial cellulose (BC) itself is white (Fig. 2a) with a 3D porous network structure (Fig. 2b, c). The color of BC turns to green (Fig. 2d) after modified with Ni-MOF. Field-emission scanning electron microscopic (FESEM) images (Fig. 2e and f) show that the BC@Ni-MOF remains the 3D porous network structure of BC. Besides, some petal-like Ni-MOFs sizing in ~2 μm, which is the reason for the color change, are readily observed in BC@Ni-MOF. Fig. 2g shows the product of BC@Ni-MOF after high temperature treatment (i.e., CNF@C-Ni), which exhibits an excellent light weight property and could be supported by stamens. FESEM images of CNF@C-Ni show that diameter of the obtained carbon fiber (~60 nm) is smaller than that of the pristine BC fiber (~90 nm) due to the elimination of organic components on the BC surface. The size of the flower-like C-Ni in CNF@C-Ni is similar to that of petal-like Ni-MOF in BC@Ni-MOF (Fig. 2e and h). In addition, CNF@C-Ni presents an excellent multi-layer structure, which is beneficial to improve impedance matching and promotes more microwave scattering.

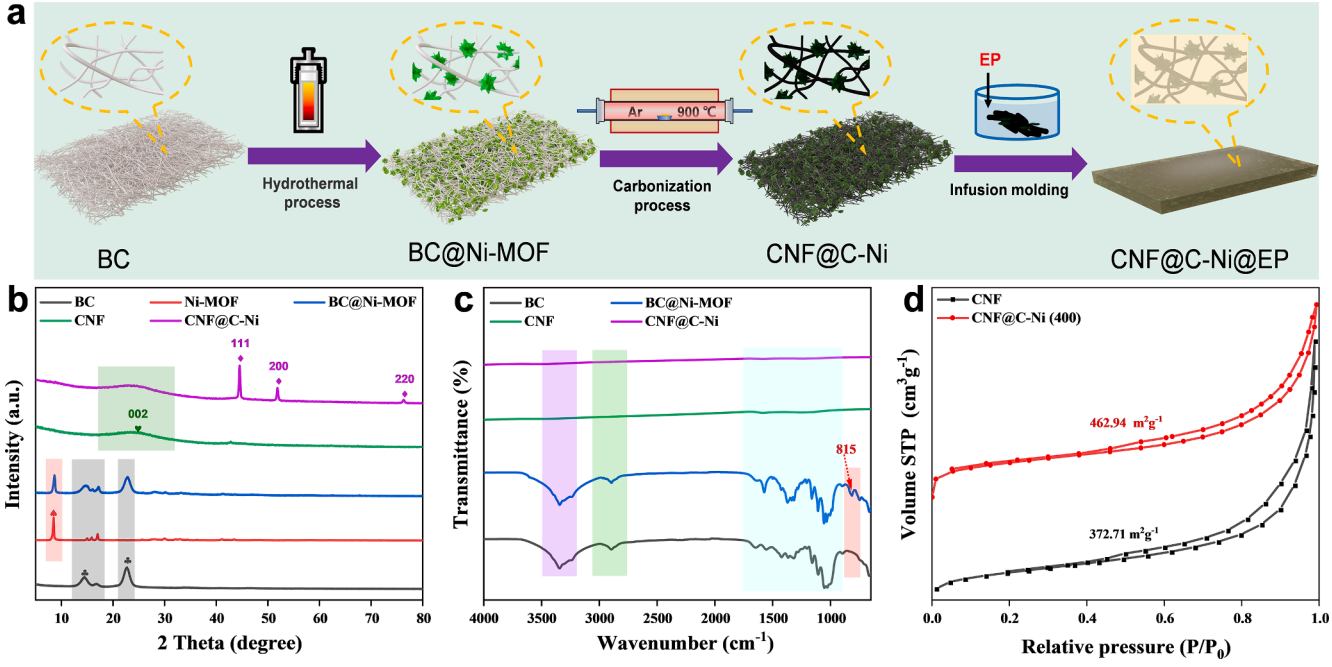

Fig. 1. (a) Schematic diagram of the preparation process for CNF@C-Ni/EP. (b) XRD patterns of BC, Ni-MOF, BC@Ni-MOF, CNF and CNF@C-Ni. (c) FTIR analysis of BC, BC@Ni-MOF, CNF and CNF@C-Ni. (d) Nitrogen adsorption–desorption curves of CNF and CNF@C-Ni (400) samples.

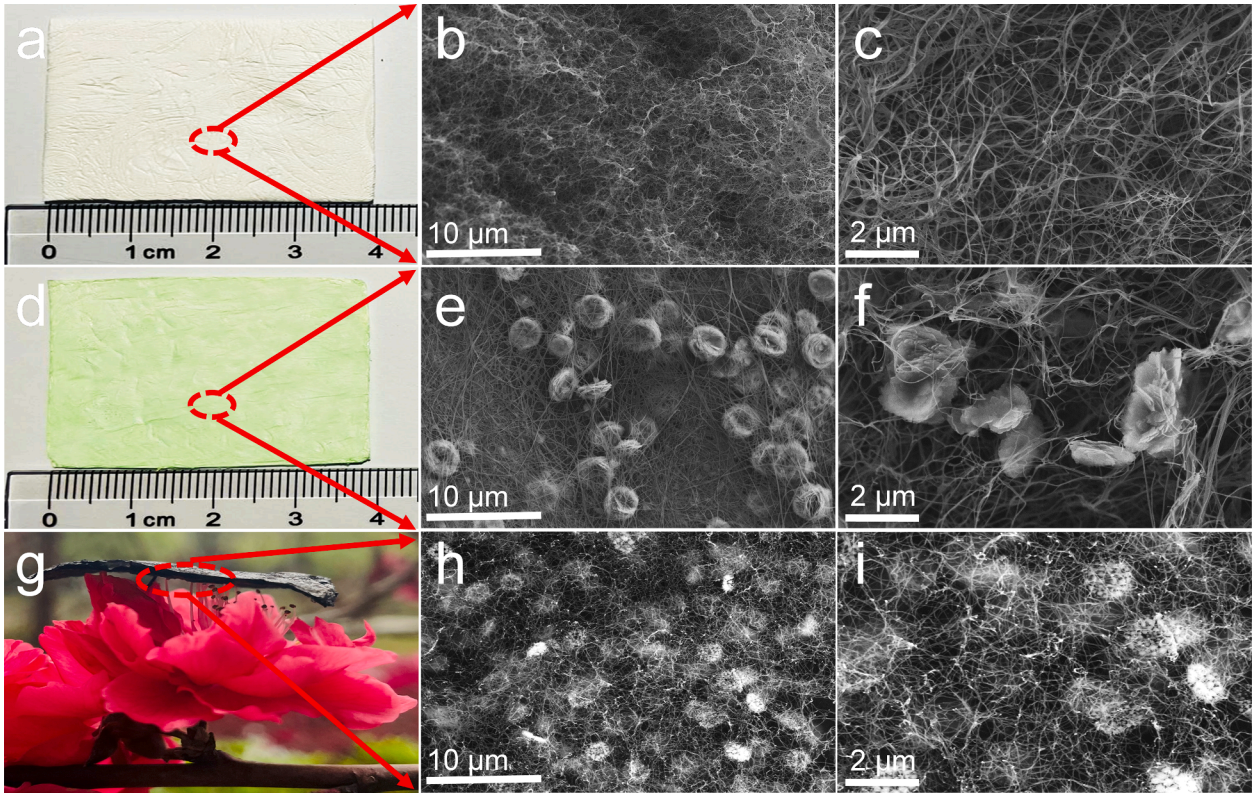

Fig. 2. Digital images of (a) BC, (d) BC@Ni-MOF and (g) CNF@C-Ni supported by stamens. Field-emission scanning electron microscopic (FESEM) images of (b, c) BC, (e, f) BC@Ni-MOF and (h, i) CNF@C-Ni.

3.2. Electromagnetic wave absorption performance

In order to study the electromagnetic wave absorption properties of CNF and CNF@C-Ni, the electromagnetic parameters of CNF and CNF@C-Ni were measured by the coaxial method, and the reflection loss (*RL*) values of the samples were calculated using the following formulas [44,45]:

$$Z_{in} = Z_0\sqrt{\frac{\mu_r}{\varepsilon_r}}tanh\left[j\left(\frac{2\pi fd}{c}\right)\sqrt{\mu_r\varepsilon_r}\right] \quad (1)$$

$$RL(dB) = 20log\left|\frac{Z_{in}-Z_0}{Z_{in}+Z_0}\right| \quad (2)$$

where, Z_{in} and Z_0 are the input impedance in free space and the characteristic impedance of absorber materials, respectively. μ_r is complex permeability ($\mu_r = \mu' - j\mu''$), ε_r is complex permittivity ($\varepsilon_r = \varepsilon' - j\varepsilon''$). f is frequency of the electromagnetic wave, d is the thickness of absorber, and c is speed of the electromagnetic wave in free space (i.e., speed of light), respectively. *RL* value lower than −10 dB is usually needed for electromagnetic wave absorption materials, which means that more than 90% of electromagnetic waves could be absorbed. The electromagnetic wave frequency range with the *RL* values lower than −10 dB is defined as effective absorption bandwidth (EAB).

Fig. 3a-d show the RL values for CNF, CNF@C-Ni (200), CNF@C-Ni (400) and CNF@C-Ni (600), respectively. The thickness of these samples varies from 1 to 5 mm, and the measuring frequency ranges from 2 to 18 GHz with a frequency resolution of 5 MHz. The CNF shows a relatively poor microwave absorption performance with a lowest RL value of −6 dB, which can be ascribed to impedance mismatching originated from exorbitant conductivity of CNF, thus considerable electromagnetic waves were reflected on the surface of CNF rather than absorbed. The electromagnetic wave absorption performance of CNF is largely enhanced by introducing of micro C-Ni flower. In which, CNF@C-Ni (400) shows the lowest RL of −49.77 dB (Fig. 3g) at 13.44 GHz, and EBA reaches to 5.44 GHz from 12.08 to 17.52 GHz, Fig. 3e. As we all know, microwave absorbing materials are required to meet the characteristics of thin, light, wide, and strong [46]. Therefore, in addition to ensuring strong microwave loss capability and wide absorption bandwidth, thickness and filling volume are also important parameters that need to be considered. As shown in Fig. 3f, a high RL values of −37.5 dB combined with an EAB value of 3.68 GHz can be reached in CNF@C-Ni (400) when its thickness is only 1.8 mm. Such a high RL value can be further increased to −49.77 dB with the thickness increasing to 2.2 mm. It is noted that the electromagnetic wave absorption performance is achieved with only 5 wt% of CNF@C-Ni (400) (Fig. S3). We then compared our absorber with other carbon-based microwave absorbers by considering content-mass ratio, thickness as well as the EMW absorption performance, Fig. 3h. The excellent comprehensive capability enables CNF@C-Ni (400) to provide a broad application value for light-weight packaging materials in electromagnetic protection [47–54].

To better understand the mechanism in the difference of EMW absorption performance of the samples, we analyzed their electromagnetic parameters (e.g., permittivity, permeability). The frequency dependent real parts ε' and imaginary parts ε'' of complex permittivities for CNF, CNF@C-Ni (200), CNF@C-Ni (400) and CNF@C-Ni (600) are depicted in Fig. 4a and b, respectively. The ε' and ε'' gradually decrease with increase of frequency owing to the relaxation phenomenon caused by electric dipole polarization, this trend with frequency is conducive to increasing the effective bandwidth of EMW absorption. In addition, the ε' and ε'' reduce obviously with increasing content of C-Ni in CNF@C-Ni. indicating that the dielectric loss performance of CNF@C-Ni composites is mainly determined by the content of C-Ni. For example, the ε'' at 2 GHz is 34.21, 6.97, 5.88 and 1.68 for CNF, CNF@C-Ni (200), CNF@C-Ni (400) and CNF@C-Ni (600), respectively. We noted that the ε' and ε'' values of individual C-Ni are relatively low in entire

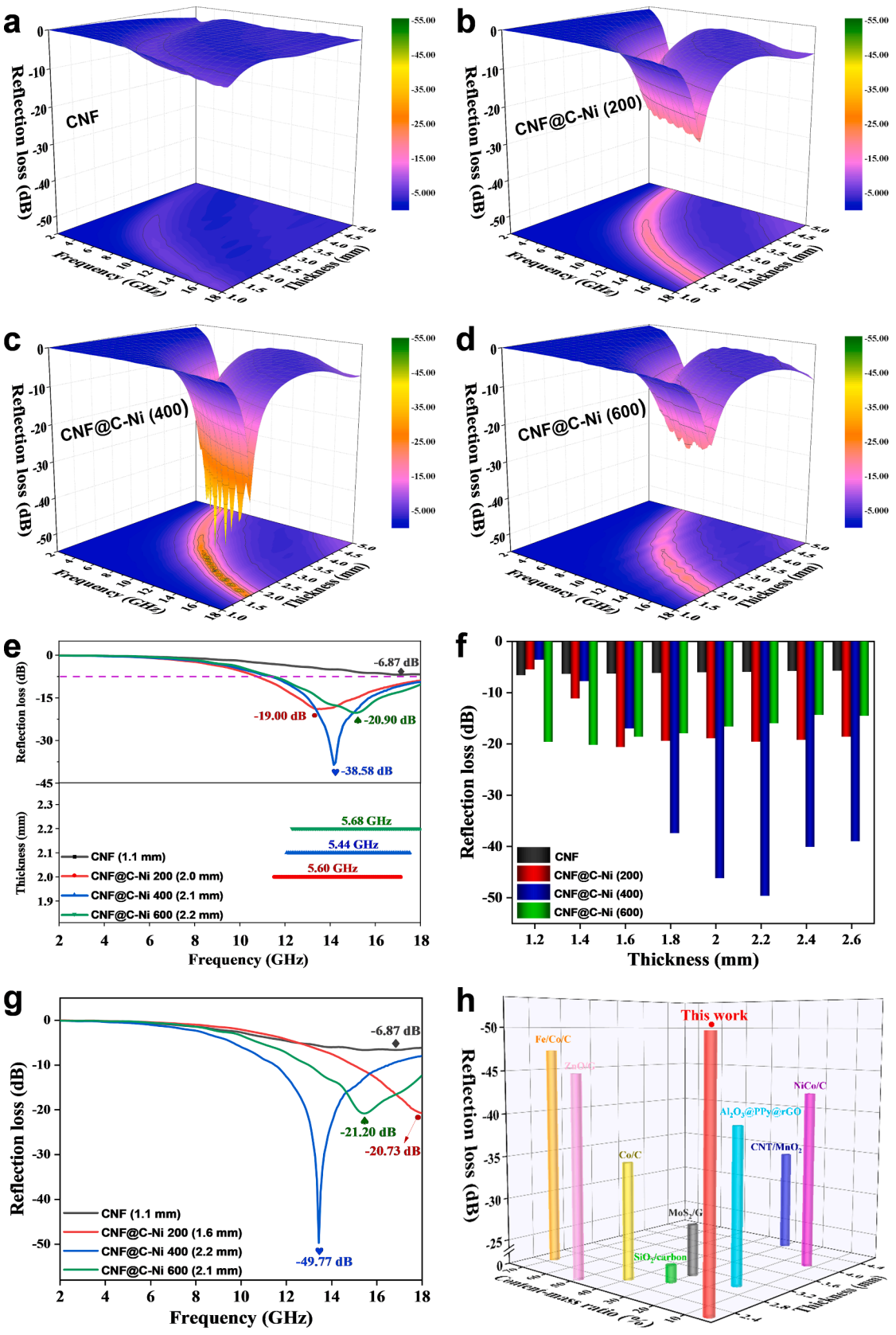

Fig. 3. Three-dimensional (3D) representations of the RL for (a) CNF, (b) CNF@C-Ni(200), (c) CNF@C-Ni(400) and (d) CNF@C-Ni(600) with the content of 5 wt%, (e) Maximum EAB values of the samples, (f) Minimum RL values of the samples with thicknesses of 1.2–2.6 mm, (g) Minimum RL values of the samples, (h) Comparison of the content-mass ratio, thickness and minimum RL of other carbon-based microwave absorbers reported in recent literatures.

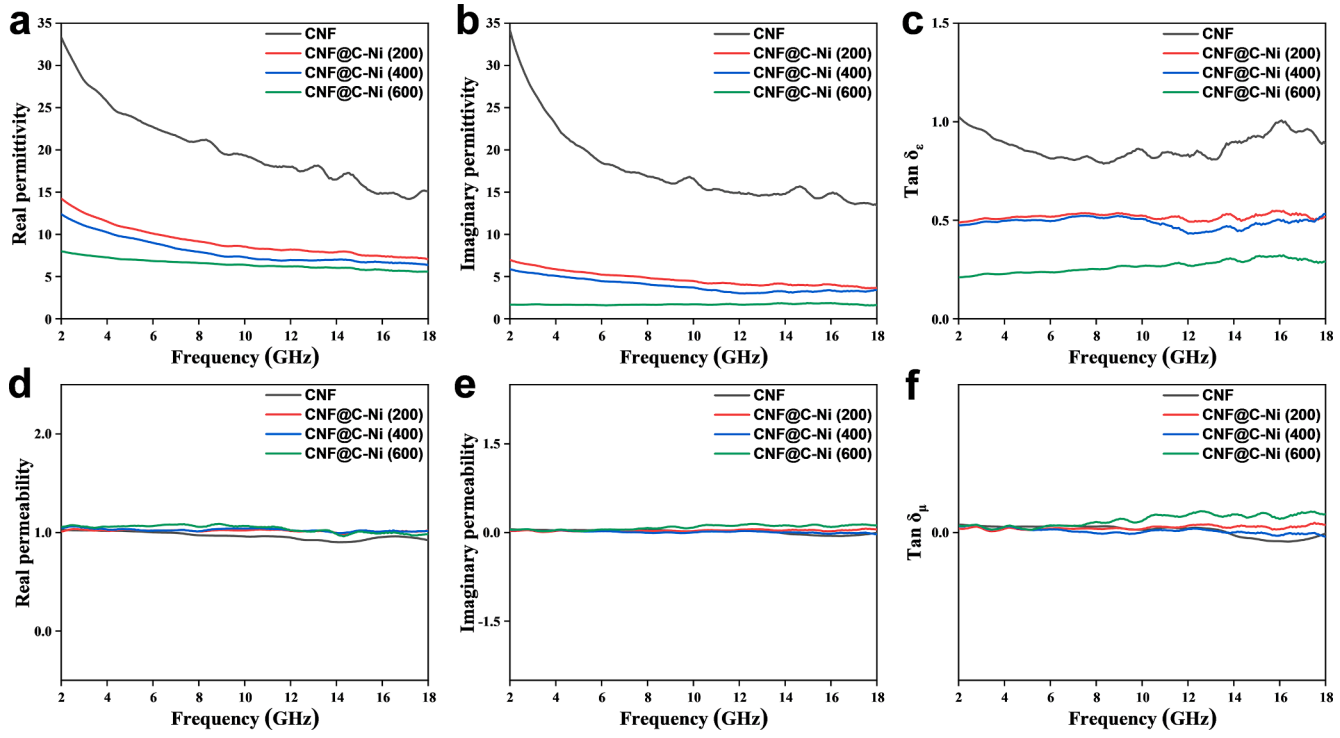

Fig. 4. (a) Real parts of permittivities, (b) imaginary parts of permittivities, (c) dielectric loss tangent, (d) real parts of permeabilities (e) imaginary parts of permeabilities and (f) magnetic loss tangent of CNF, CNF@C-Ni(200), CNF@C-Ni(400) and CNF@C-Ni(600), respectively.

frequency range, especially the ε'' values are around 0 (Fig. S4). It means that the dielectric loss caused by C-Ni nanoflowers is relatively low. Therefore, as the content of C-Ni increased in CNF@C-Ni, the content of CNF with high dielectric loss was relatively reduced, resulting in a significant decrease in the value of ε''. In addition, there are multiple fluctuation peaks in ε' and ε'' curves, indicating that multiple relaxation phenomena occur. This might be related to the interface polarization and dipolar polarization in the materials. Where the dipolar polarization can be attributed to asymmetric distribution of charge at defects in CNF or C-Ni, and interface polarization might occur in a heterogeneous interface with different charge accumulation at the boundary between CNF and C-Ni [53,55]. Further, it can be confirmed by Cole-Cole diagram (as shown in Fig. S5). Compared with pure CNF, CNF@C-Ni (400) has multiple semicircles in Cole-Cole diagram, indicating that there are multiple Debye relaxations [54]. It is worth noting that there is an obvious straight line at the end of the curve, indicating that the three-dimensional CNF conductive network has a certain conductivity loss ability provided by the microwave absorber.

Fig. 4d and e show the real parts (μ') and imaginary parts (μ'') of permeability values of all samples. The μ' values are about 1.0, while the μ'' values are stabilized around 0.2 for all the samples. Such a low μ'' indicates magnetic loss in these samples is marginal compared to dielectric loss, which can be ascribed to the small size and content of nickel nanoparticles in the samples. Interestingly, μ'' has a negative value at high frequencies, and appearance of complex permeability might be attributed to magnetic energy radiation generated by sample in an electromagnetic field. Generally speaking, in 2–18 GHz, magnetic loss mainly comes from natural resonance, exchange resonance and eddy current loss effects. In addition, multiple fluctuations in C_0 ($C_0 = \mu''(\mu')^{-2}f^{-1}$) throughout the test range were observed, indicating that there are multiple magnetic loss mechanisms rather than only eddy current loss. For instance, the vibration peaks at ~6 GHz and ~12 GHz are caused by natural resonance and exchange resonance [56] (Fig. S6). Moreover, by comparing the dielectric loss tangent (Fig. 4c) and magnetic loss tangent (Fig. 4f), the dielectric loss tangent values are much larger than the magnetic loss tangent value, thus the dielectric loss is the main contributor for EMW absorption in our samples.

Attenuation constant α refers to material's intrinsic attenuation ability for electromagnetic waves, which can be calculated by following equation [57]:

$$\alpha = \frac{\sqrt{2}\pi f}{c}\sqrt{(\mu''\varepsilon'' - \mu'\varepsilon') + \sqrt{(\mu''\varepsilon'' - \mu'\varepsilon')^2 + (\mu'\varepsilon'' + \mu''\varepsilon')^2}} \quad (3)$$

Typically, a larger attenuation constant value means a better ability to consume electromagnetic waves of the material. However, for high EMW absorption performance, a high impedance matching ($Z = |Z_{in}/Z_0|$) is also needed, because a high impedance matching means more EMW can easily enter the inside of the material and be effectively dissipated. As shown in the Fig. 5a, although the α value of CNF is higher than that of CNF-C-Ni composite material, its overall microwave absorption capacity is very low due to its low impedance matching (i.e., $Z = 0.5$, Fig. S7). As a result, more electromagnetic waves are reflected rather than absorbed. The low Z value increases with increasing content of C-Ni, which are 0.8, 1 and 1.1 for CNF@C-Ni (200), CNF@C-Ni (400) and CNF@C-Ni (600), respectively (Fig. 5c, d, e). It is generally believed that impedance of absorber and air is almost the same when $Z = 1$, which means that more electromagnetic waves can easily enter absorber from the air instead of being reflected [58]. Therefore, CNF@C-Ni (400) with a suitable attenuation constant and good impedance matching shows the highest EMW absorption performance.

Based on the above analysis, the main EMW wave attenuation mechanisms of CNF@C-Ni are summarized in Fig. 5b. Firstly, absorption mechanisms for high-performance microwave absorption materials are usually related to two aspects: impedance matching and attenuation ability. Good impedance matching signifies that microwave can fully enter into the materials, which is an essential prerequisite for microwave absorption. Outstanding attenuation ability requires that materials can transform microwave energy into thermal or other energy for consumption. Secondly, the high specific surface area of CNF@C-Ni makes the incident microwave reflect multiple times at the active site, thereby enhancing energy dissipation [46,59]. Meanwhile, interface

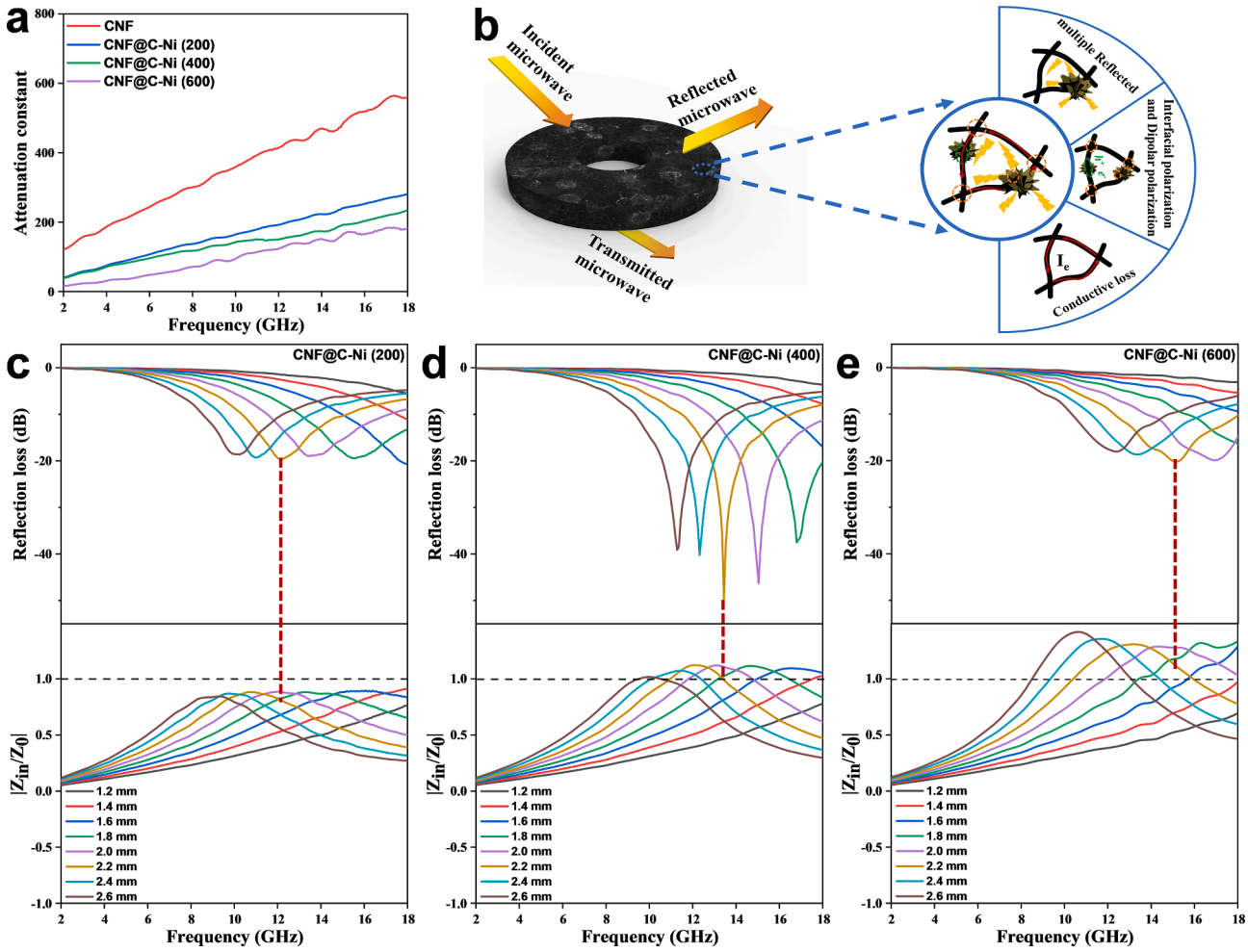

Fig. 5. (a) Attenuation constant, (b) Schematic diagram of the EMW absorption mechanisms of CNF@C-Ni. The reflection loss and the impedance matching characteristics of CNF@C-Ni(200) (c), CNF@C-Ni(400) (d) and CNF@C-Ni(600) (e) with different thickness.

polarization and dipolar polarization caused by the multiple interfaces between CNF and C-Ni and the accumulation of different charges at the interface, further enhances the attenuation of microwaves. In addition, the high aspect ratio CNF three-dimensional network structure constitutes a conductive path to optimize the conduction loss, thereby improving the microwave loss efficiency to a certain extent.

3.3. Thermal conductivity and thermal management property

We measured the thermal conductivity of EP and CNF@C-Ni/EP by transient test method. As shown in Fig. 6a, the thermal conductivity is only ~0.18 $W{\cdot}m^{-1}K^{-1}$ for pure EP at room temperature, which rises to ~0.5 $W{\cdot}m^{-1}K^{-1}$ for CNF@C-Ni/EP composite. It is very exciting to be able to achieve such a high thermal conductivity when the filling content of CNF@C-Ni is only 5 wt%, which is an important guarantee to meet the lightweight requirements of epoxy resin based electronic packaging materials [60,61]. Generally, the efficiency η of thermally conductive fillers is evaluated according to the thermal conductivity enhancement (TCE) [62]:

$$\eta(\%) = \frac{100(\kappa - \kappa_m)}{\kappa_m} \quad (4)$$

where the thermal conductivity of the composite material is represented by κ, as well as κ_m is the thermal conductivity of the matrix material. We calculated the TCE value of CNF@C-Ni/EP using equation (4), which reaches ~178. Such a high TEC value is much higher than that of other epoxy resin-based composites with similar filling content as we listed in Table 1. The main reason for this high thermal conductivity enhancement is that CNF@C-Ni not only has a high aspect ratio and a high thermal conductivity itself, but also perfectly retains the 3D network structure of BC, thus providing a good 3D heat propagation path to epoxy.

In order to practically verify the thermal management capability of CNF@C-Ni/EP composites, we tested the changes in upper surface temperature of EP and CNF@C-Ni/EP during heating and cooling using an infrared thermal imager. When we placed pure EP and CNF@C-Ni/EP on a heating table with a temperature of ~49 °C, the upper surface of CNF@C-Ni/EP can be heated to 47 °C in 60 s, while the pure EP is only 38.06 °C (Fig. 6b and e), reflecting the higher thermal conductivity of CNF@C-Ni/EP composite than EP. Similarly, when we placed EP and CNF@C-Ni/EP which had the same initial temperature (~50 °C) in air (~22 °C) for cooling, the upper surface temperature of CNF@C-Ni/EP dropped faster than that of EP (Fig. 6c and f). Fig. 6d shows the heat conduction mechanism of CNF@C-Ni/EP composite, which mainly depends on the 3D CNF@C-Ni in EP. The low filling volume and high thermal conductivity enable CNF@C-Ni/EP to be a promising electronic packaging material.

4. Conclusion

This work demonstrates a promising dual-functionated epoxy resin based electronic packaging material for highly integrated electronic devices, which was obtained by filling 3D CNF@C-Ni network skeleton

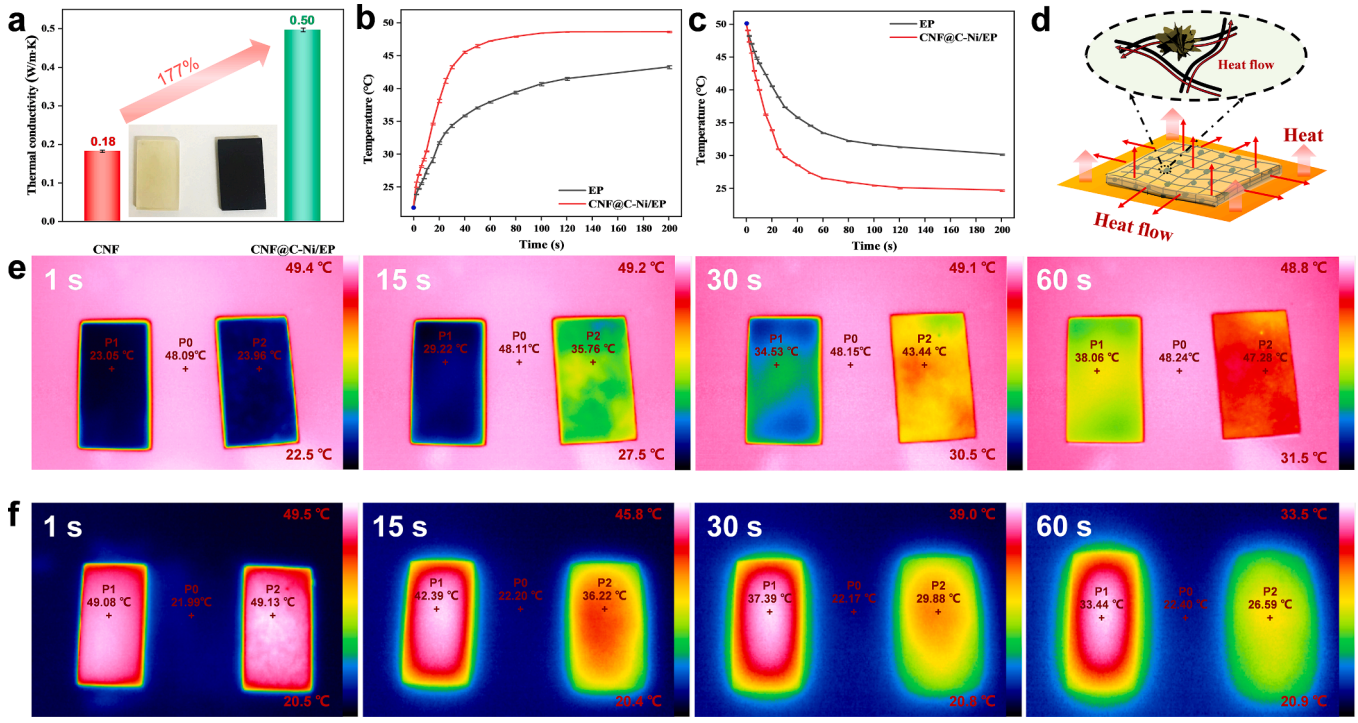

Fig. 6. (a) Thermal conductivities of PE and CNF@C-Ni/EP, (b) The surface temperature of EP and CNF@C-Ni/EP changes with time, (e) the corresponding IR images. (c) The surface temperature of EP and CNF@C-Ni/EP changes with time and (f) the corresponding IR images. (d) Schematic diagram of the heat transfer in CNF@C-Ni composites.

Table 1
Comparison of thermal conductivity (κ) of our CNF@C-Ni/EP composite with other epoxy-based composites.

Fillers	Loading (wt %)	κ of Epoxy resins ($W·m^{-1}K^{-1}$)	κ of Composite material ($W·m^{-1}K^{-1}$)	η (%)	Ref.
NGF/BFs	10	0.16	0.39	140	[63]
VmhBN	5	0.15	0.2	30	[64]
RmhBN	5	0.15	0.3	100	[64]
CNT/MoS_2	5	0.2	0.33	70	[65]
GBN50	5	0.2	0.48	140	[66]
Al_2O_3	5	0.17	~0.25	50	[21]
Diamond	29.4	0.17	0.35	110	[67]
MF-10	15	0.22	0.46	110	[68]
SiO_2	20	0.18	0.25	39	[21]
CNF@Ni-C	5	0.18	0.5	178	This work

in EP using a vacuum impregnation strategy. The filler CNF@C-Ni was prepared by high-temperature carbonizing flower-like Ni-MOF embellished bacterial cellulose (BC, a natural, non-toxic, low-cost biological material). In which, the CNF remains the 3D network structure of BC, the C-Ni particles size in ~2 μm with a multilayer structure. On one hand, the C-Ni particles increase the impedance matching of pure CNF as well as the CNF/EP composites, thus a high electromagnetic wave absorption performance has been achieved for CNF@C-Ni/EP composites. Specifically, when the CNF@C-Ni filling amount is 5 wt%, the minimum reflection loss value is up to −49.77 dB at a frequency of 13.44 GHz and a thickness of 2.2 mm, and the maximum effective bandwidth reaches 5.44 GHz in the frequency range of 12.08–17.52 GHz. On the other hand, due to the introduction of 3D CNF heat transfer network, the CNF@C-Ni/EP also exhibits a high thermal conductivity of 0.5 $W·m^{-1}K^{-1}$ at room temperature, an increase of ~280% comparing with pure EP. The lightweight, high electromagnetic wave absorption performance and good management capability promote the CNF@C-Ni/EP composite to be an ideal electronic packaging material.

Declaration of Competing Interest

The authors declare that they have no known competing financial interests or personal relationships that could have appeared to influence the work reported in this paper.

Acknowledgements

This work was supported by the National Natural Science Foundation of China under Grant No. 52002137, 51772109, 51872102 and 51802070, the Fundamental Research Funds for the Central Universities under Grant No. 2021XXJS008 and 2018KFYXKJC002, Graduates' Innovation Fund, Huazhong University of Science and Technology under Grant No. 2020yjsCXCY022. The technical assistance from the Analytical and Testing Center of HUST is likewise gratefully acknowledged.

Appendix A. Supplementary material

Supplementary data to this article can be found online at https://doi.org/10.1016/j.cej.2021.131608.

References

[1] A.L. Moore, L. Shi, Emerging challenges and materials for thermal management of electronics, Mater. Today 17 (4) (2014) 163–174.
[2] J. Song, X. Feng, Y. Huang, Mechanics and thermal management of stretchable inorganic electronics, Natl. Sci. Rev. 3 (1) (2016) 128–143.
[3] R.C. Che, L.M. Peng, X.F. Duan, Q. Chen, Liang, XL, Microwave absorption enhancement and complex permittivity and permeability of Fe encapsulated within carbon nanotubes, Adv. Mater. 16 (5) (2004) 401–405.
[4] X. Liu, Y. Li, X. Sun, W. Tang, G. Deng, Y. Liu, Z. Song, Y. Yu, R. Yu, L. Dai, Off/on switchable smart electromagnetic interference shielding aerogel, Matter 4 (2021) 1735–1747.

[5] Y. Cui, Z. Qin, H. Wu, M. Li, Y. Hu, Flexible thermal interface based on self-assembled boron arsenide for high-performance thermal management, Nat. Commun. 12 (1) (2021) 1–7.

[6] S. Wan Cho, K. Han, Y. Yi, S.J. Kang, K.H. Yoo, K. Jeong, C.N. Whang, Thermal oxidation study on lead-free solders of Sn-Ag-Cu and Sn-Ag-Cu-Ge, Adv. Eng. Mater. 8 (1–2) (2006) 111–114.

[7] D. Ji, T. Li, W. Hu, H. Fuchs, Recent progress in aromatic polyimide dielectrics for organic electronic devices and circuits, Adv. Mater. 31 (15) (2019) 1806070.

[8] Z. Xu, M. Wu, W. Gao, H. Bai, A. Transparent, Skin-inspired composite film with outstanding tear resistance based on flat silk cocoon, Adv. Mater. 32 (34) (2020) 2002695.

[9] X. Huang, C. Zhi, P. Jiang, D. Golberg, Y. Bando, T. Tanaka, Polyhedral oligosilsesquioxane-modified boron nitride nanotube based epoxy nanocomposites: an ideal dielectric material with high thermal conductivity, Adv. Funct. Mater. 23 (14) (2013) 1824–1831.

[10] Y. Tian, Q. Wang, L. Shen, Z. Cui, L. Kou, J. Cheng, J. Zhang, A renewable resveratrol-based epoxy resin with high Tg, excellent mechanical properties and low flammability, Chem. Eng. J. 383 (2020) 123124.

[11] X. Jing, J. Wei, Y. Liu, B. Song, Y. Liu, Deployment analysis of aramid fiber reinforced shape-memory epoxy resin composites, Eng. Sci. 11 (2) (2020) 44–53.

[12] Y. Feng, J. Hu, Y. Xue, C. He, X. Zhou, X. Xie, Y. Ye, Y.-W. Mai, Simultaneous improvement in the flame resistance and thermal conductivity of epoxy/Al_2O_3 composites by incorporating polymeric flame retardant-functionalized graphene, J. Mater. Chem. A 5 (26) (2017) 13544–13556.

[13] F. Shahzad, M. Alhabeb, C.B. Hatter, B. Anasori, S.M. Hong, C.M. Koo, Y. Gogotsi, Electromagnetic interference shielding with 2D transition metal carbides (MXenes), Science 353 (6304) (2016) 1137–1140.

[14] A. Iqbal, F. Shahzad, K. Hantanasirisakul, M.-K. Kim, J. Kwon, J. Hong, H. Kim, D. Kim, Y. Gogotsi, C.M. Koo, Anomalous absorption of electromagnetic waves by 2D transition metal carbonitride Ti3CNTx (MXene), Science 369 (6502) (2020) 446–450.

[15] Q. Yan, W. Dai, J. Gao, X. Tan, L. Lv, J. Ying, X. Lu, J. Lu, Y. Yao, Q. Wei, Ultrahigh-aspect-ratio boron nitride nanosheets leading to superhigh in-plane thermal conductivity of foldable heat spreader, ACS Nano 15 (2021) 6489–6498.

[16] G. Pan, Y. Yao, X. Zeng, J. Sun, J. Hu, R. Sun, J.-B. Xu, C.-P. Wong, Learning from natural nacre: constructing layered polymer composites with high thermal conductivity, ACS Appl. Mater. Interfaces 9 (38) (2017) 33001–33010.

[17] W. Bian, T. Yao, M. Chen, C. Zhang, T. Shao, Y. Yang, The synergistic effects of the micro-BN and nano-Al2O3 in micro-nano composites on enhancing the thermal conductivity for insulating epoxy resin, Compos. Sci. Technol. 168 (2018) 420–428.

[18] Y. Jiang, X. Shi, Y. Feng, S. Li, X. Zhou, X. Xie, Enhanced thermal conductivity and ideal dielectric properties of epoxy composites containing polymer modified hexagonal boron nitride, Compos. Part A Appl. Sci. Manuf. 107 (2018) 657–664.

[19] C. Yu, J. Zhang, Z. Li, W. Tian, L. Wang, J. Luo, Q. Li, X. Fan, Y. Yao, Enhanced through-plane thermal conductivity of boron nitride/epoxy composites, Compos. A Appl. Sci. Manuf. 98 (2017) 25–31.

[20] J. Li, P. Zhang, H. He, S. Zhai, Y. Xian, W. Ma, L. Wang, Enhanced thermal transport properties of epoxy resin thermal interface materials, ES Energy Environ. 4 (6) (2019) 41–47.

[21] R. Kochetov, T. Andritsch, P.H. Morshuis, J.J. Smit, Thermal and electrical behaviour of epoxy-based microcomposites filled with Al2O3 and SiO2 particles, in: 2010 IEEE International Symposium on Electrical Insulation, IEEE, 2010, pp. 1–5.

[22] E. Hwang, S. Adam, S.D. Sarma, Carrier transport in two-dimensional graphene layers, Phys. Rev. Lett. 98 (18) (2007) 186806.

[23] S. Chen, Q. Wu, C. Mishra, J. Kang, H. Zhang, K. Cho, W. Cai, A.A. Balandin, R. S. Ruoff, Thermal conductivity of isotopically modified graphene, Nat. Mater. 11 (3) (2012) 203–207.

[24] Y. Yao, J. Sun, X. Zeng, R. Sun, J.B. Xu, C.P. Wong, Construction of 3D skeleton for polymer composites achieving a high thermal conductivity, Small 14 (13) (2018) 1704044.

[25] X. Xu, R. Hu, M. Chen, J. Dong, B. Xiao, Q. Wang, H. Wang, 3D boron nitride foam filled epoxy composites with significantly enhanced thermal conductivity by a facial and scalable approach, Chem. Eng. J. 397 (2020) 125447.

[26] M. Qin, Y. Xu, R. Cao, W. Feng, L. Chen, Efficiently controlling the 3D thermal conductivity of a polymer nanocomposite via a hyperelastic double-continuous network of graphene and sponge, Adv. Funct. Mater. 28 (45) (2018) 1805053.

[27] Y. Zhang, Y. Huang, T. Zhang, H. Chang, P. Xiao, H. Chen, Z. Huang, Y. Chen, Broadband and tunable high-performance microwave absorption of an ultralight and highly compressible graphene foam, Adv. Mater. 27 (12) (2015) 2049–2053.

[28] L. Wang, X. Jia, Y. Li, F. Yang, L. Zhang, L. Liu, X. Ren, H. Yang, Synthesis and microwave absorption property of flexible magnetic film based on graphene oxide/carbon nanotubes and Fe_3O_4 nanoparticles, J. Mater. Chem. A 2 (36) (2014) 14940–14946.

[29] B. Zhong, Y. Cheng, M. Wang, Y. Bai, X. Huang, Y. Yu, H. Wang, G. Wen, Three dimensional hexagonal boron nitride nanosheet/carbon nanotube composites with light weight and enhanced microwave absorption performance, Compos. Part A : Appl. Sci. Manuf. 112 (2018) 515–524.

[30] Y.-H. Chen, Z.-H. Huang, M.-M. Lu, W.-Q. Cao, J. Yuan, D.-Q. Zhang, M.-S. Cao, 3D Fe_3O_4 nanocrystals decorating carbon nanotubes to tune electromagnetic properties and enhance microwave absorption capacity, J. Mater. Chem. A 3 (24) (2015) 12621–12625.

[31] C. Song, X. Yin, M. Han, X. Li, Z. Hou, L. Zhang, L. Cheng, Three-dimensional reduced graphene oxide foam modified with ZnO nanowires for enhanced microwave absorption properties, Carbon 116 (2017) 50–58.

[32] S. Xiao, H. Mei, D. Han, K.G. Dassios, L. Cheng, Ultralight lamellar amorphous carbon foam nanostructured by SiC nanowires for tunable electromagnetic wave absorption, Carbon 122 (2017) 718–725.

[33] X. Wu, C. Fu, Z. Zhang, Chiral absorbers based on polarization conversion and excitation of magnetic polaritons, ES Energy Environ. 8 (2) (2020) 5–14.

[34] X. Xu, S. Shi, Y. Tang, G. Wang, M. Zhou, G. Zhao, X. Zhou, S. Lin, F. Meng, Growth of NiAl-layered double hydroxide on graphene toward excellent anticorrosive microwave absorption application, Adv. Sci. 8 (5) (2021) 2002658.

[35] M.M. Pérez-Madrigal, M.G. Edo, C. Alemán, Powering the future: application of cellulose-based materials for supercapacitors, Green Chem. 18 (22) (2016) 5930–5956.

[36] Z. Wang, P. Tammela, M. Strømme, L. Nyholm, Cellulose-based supercapacitors: material and performance considerations, Adv. Energy Mater. 7 (18) (2017) 1700130.

[37] L.F. Chen, Z.H. Huang, H.W. Liang, H.L. Gao, S.H. Yu, Three-dimensional heteroatom-doped carbon nanofiber networks derived from bacterial cellulose for supercapacitors, Adv. Funct. Mater. 24 (32) (2014) 5104–5111.

[38] Q. Gao, Y. Pan, G. Zheng, C. Liu, C. Shen, X. Liu, Flexible multilayered MXene/thermoplastic polyurethane films with excellent electromagnetic interference shielding, thermal conductivity, and management performances, Adv. Compos. Hybrid Mater. 4 (2) (2021) 274–285.

[39] A. Rastegarpanah, M. Rezaei, F. Meshkani, K. Zhang, X. Zhao, W. Pei, Y. Liu, J. Deng, H. Arandiyan, H. Dai, Influence of group VIB metals on activity of the Ni/MgO catalysts for methane decomposition, Appl. Catal. B 248 (2019) 515–525.

[40] Y. Fei, M. Liang, T. Zhou, Y. Chen, H. Zou, Unique carbon nanofiber@ Co/C aerogel derived bacterial cellulose embedded zeolitic imidazolate frameworks for high-performance electromagnetic interference shielding, Carbon 167 (2020) 575–584.

[41] H. Gao, L. Ding, H. Bai, A. Liu, S. Li, L. Li, Pitch-based hyper-cross-linked polymers with high performance for gas adsorption, J. Mater. Chem. A 4 (42) (2016) 16490–16498.

[42] J. Chen, X. Wang, Y. Huang, S. Lv, X. Cao, J. Yun, D. Cao, Adsorption removal of pollutant dyes in wastewater by nitrogen-doped porous carbons derived from natural leaves, Eng. Sci. 5 (9) (2018) 30–38.

[43] Q. Liu, X. Liu, H. Feng, H. Shui, R. Yu, Metal organic framework-derived Fe/carbon porous composite with low Fe content for lightweight and highly efficient electromagnetic wave absorber, Chem. Eng. J. 314 (2017) 320–327.

[44] L. Huang, J. Li, Z. Wang, Y. Li, X. He, Y. Yuan, Microwave absorption enhancement of porous C@ $CoFe_2O_4$ nanocomposites derived from eggshell membrane, Carbon 143 (2019) 507–516.

[45] S. Kim, S. Jo, K. Gueon, K. Choi, J. Kim, K. Churn, Complex permeability and permittivity and microwave absorption of ferrite-rubber composite at X-band frequencies, IEEE Trans. Magn. 27 (6) (1991) 5462–5464.

[46] X. Li, X. Yin, C. Song, M. Han, H. Xu, W. Duan, L. Cheng, L. Zhang, Self-assembly core-shell graphene-bridged hollow MXenes spheres 3D foam with ultrahigh specific EM absorption performance, Adv. Funct. Mater. 28 (41) (2018) 1803938.

[47] Y. Wang, Y. Chen, X. Wu, W. Zhang, C. Luo, J. Li, Fabrication of MoS_2-graphene modified with Fe_3O_4 particles and its enhanced microwave absorption performance, Adv. Powder Technol. 29 (3) (2018) 744–750.

[48] M. Han, X. Yin, L. Kong, M. Li, W. Duan, L. Zhang, L. Cheng, Graphene-wrapped ZnO hollow spheres with enhanced electromagnetic wave absorption properties, J. Mater. Chem. A 2 (39) (2014) 16403–16409.

[49] X. Fan, R. Yuan, X. Li, H. Xu, L. Kong, G. Wu, L. Zhang, L. Cheng, RGO-supported core-shell SiO_2@ SiO_2/carbon microsphere with adjustable microwave absorption properties, Ceram. Int. 46 (10) (2020) 14985–14993.

[50] C. Li, J. Sui, Z. Zhang, X. Jiang, Z. Zhang, L. Yu, Microwave-assisted synthesis of tremella-like NiCo/C composites for efficient broadband electromagnetic wave absorption at 2–40 GHz, Chem. Eng. J. 375 (2019) 122017.

[51] Y. Lai, L. Lv, H. Fu, Preparation and study of Al_2O_3@ PPy@ rGO composites with microwave absorption properties, J. Alloy. Compd. 832 (2020) 152957.

[52] H. Pang, A.M. Abdalla, R.P. Sahu, Y. Duan, I.K. Puri, Low-temperature synthesis of manganese oxide-carbon nanotube-enhanced microwave-absorbing nanocomposites, J. Mater. Sci. 53 (24) (2018) 16288–16302.

[53] L. Wang, Y. Guan, X. Qiu, H. Zhu, S. Pan, M. Yu, Q. Zhang, Efficient ferrite/Co/porous carbon microwave absorbing material based on ferrite@ metal-organic framework, Chem. Eng. J. 326 (2017) 945–955.

[54] Y. Lü, Y. Wang, H. Li, Y. Lin, Z. Jiang, Z. Xie, Q. Kuang, L. Zheng, MOF-derived porous Co/C nanocomposites with excellent electromagnetic wave absorption properties, ACS Appl. Mater. Interfaces 7 (24) (2015) 13604–13611.

[55] B. Zhao, J. Deng, R. Zhang, L. Liang, B. Fan, Z. Bai, G. Shao, C. Park, Recent advances on the electromagnetic wave absorption properties of Ni based materials, Eng. Sci. 3 (28) (2018) 5–40.

[56] J. Ma, X. Wang, W. Cao, C. Han, H. Yang, J. Yuan, M. Cao, A facile fabrication and highly tunable microwave absorption of 3D flower-like Co_3O_4-rGO hybrid-architectures, Chem. Eng. J. 339 (2018) 487–498.

[57] K. Wang, G. Wan, G. Wang, Z. He, S. Shi, L. Wu, G. Wang, The construction of carbon-coated Fe_3O_4 yolk-shell nanocomposites based on volume shrinkage from the release of oxygen anions for wide-band electromagnetic wave absorption, J. Colloid Interface Sci. 511 (2018) 307–317.

[58] X. Xu, S. Shi, G. Wan, C. Hao, Z. He, G. Wang, Uniformly coating MnO_x nanoflakes onto carbon nanofibers as lightweight and wideband microwave absorbers with frequency-selective absorption, Mater. Des. 183 (2019) 108167.

[59] M. Han, X. Yin, X. Li, B. Anasori, L. Zhang, L. Cheng, Y. Gogotsi, Laminated and two-dimensional carbon-supported microwave absorbers derived from MXenes, ACS Appl. Mater. Interfaces 9 (23) (2017) 20038–20045.

[60] C. Chen, Y. Xue, X. Li, Y. Wen, J. Liu, Z. Xue, D. Shi, X. Zhou, X. Xie, Y.-W. Mai, High-performance epoxy/binary spherical alumina composite as underfill material for electronic packaging, Compos. Part A Appl. Sci. Manuf. 118 (2019) 67–74.
[61] R. Asmatulu, P. Bollavaram, V. Patlolla, I. Alarifi, W. Khan, Investigating the effects of metallic submicron and nanofilms on fiber-reinforced composites for lightning strike protection and EMI shielding, Adv. Compos. Hybrid Mater. 3 (1) (2020) 66–83.
[62] X. Zeng, Y. Yao, Z. Gong, F. Wang, R. Sun, J. Xu, C.P. Wong, Ice-templated assembly strategy to construct 3D boron nitride nanosheet networks in polymer composites for thermal conductivity improvement, Small 11 (46) (2015) 6205–6213.
[63] S.H. Kim, Y.-J. Heo, M. Park, B.-G. Min, K.Y. Rhee, S.-J. Park, Effect of hydrophilic graphite flake on thermal conductivity and fracture toughness of basalt fibers/epoxy composites, Compos. B Eng. 153 (2018) 9–16.
[64] Z. Lin, Y. Liu, S. Raghavan, K.-S. Moon, S.K. Sitaraman, C.-P. Wong, Magnetic alignment of hexagonal boron nitride platelets in polymer matrix: toward high performance anisotropic polymer composites for electronic encapsulation, ACS Appl. Mater. Interfaces 5 (15) (2013) 7633–7640.
[65] C. Ji, C. Yan, Y. Wang, S. Xiong, F. Zhou, Y. Li, R. Sun, C.-P. Wong, Thermal conductivity enhancement of CNT/MoS_2/graphene-epoxy nanocomposites based on structural synergistic effects and interpenetrating network, Compos. B Eng. 163 (2019) 363–370.
[66] J. Ren, Q. Li, L. Yan, L. Jia, X. Huang, L. Zhao, Q. Ran, M. Fu, Enhanced thermal conductivity of epoxy composites by introducing graphene@ boron nitride nanosheets hybrid nanoparticles, Mater. Des. 191 (2020) 108663.
[67] Y.-X. Fu, Z.-X. He, D.-C. Mo, S.-S. Lu, Thermal conductivity enhancement with different fillers for epoxy resin adhesives, Appl. Therm. Eng. 66 (1–2) (2014) 493–498.
[68] L. Wang, H. Qiu, C. Liang, P. Song, Y. Han, Y. Han, J. Gu, J. Kong, D. Pan, Z. Guo, Electromagnetic interference shielding MWCNT-Fe_3O_4@ Ag/epoxy nanocomposites with satisfactory thermal conductivity and high thermal stability, Carbon 141 (2019) 506–514.